Effect of Oxygen Interstitial Ordering on Multiple Order Parameters in Rare Earth Ferrite

Yang Zhang,[1,‡] Wenbin Wang,[2,‡] Wandong Xing,[1,‡] Shaobo Cheng,[1] Shiqing Deng,[1] Manuel Angst,[3] Chu-Ping Yu,[1,6] Fanli Lan,[5] Zhiying Cheng,[1] David Mandrus,[4] Brian Sales,[4] Jian Shen,[2,5] Xiaoyan Zhong,[1] Nyan-Hwa Tai,[6] Rong Yu,[1,†] and Jing Zhu[1,*]

[1]*National Center for Electron Microscopy in Beijing, Key Laboratory of Advanced Materials (MOE), The State Key Laboratory of New Ceramics and Fine Processing, School of Materials Science and Engineering, Tsinghua University, Beijing 100084, People's Republic of China*

[2]*Institute of Nanoelectronic Devices and Quantum Computing, Fudan University, Shanghai 200433, China*

[3]*Jülich Centre for Neutron Science JCNS and Peter Grünberg Institut PGI, JARA-FIT, Forschungszentrum Jülich GmbH, 52425 Jülich, Germany*

[4]*Oak Ridge National Laboratory, Oak Ridge, Tennessee 37831, USA*

[5]*State Key Laboratory of Surface Physics and Department of Physics, Fudan University, Shanghai 200433, China*

[6]*Department of Materials Science and Engineering National Tsing-Hua University, Hsinchu 30013, Taiwan*

(Received 17 March 2019; revised manuscript received 9 September 2019; published 11 December 2019)

Oxygen interstitials and vacancies play a key role in modulating the microstructure and properties of nonstoichiometric oxide systems, such as those used for superconductors and multiferroics. Key to understanding the tuning mechanisms resulting from oxygen doping is a knowledge of the precise positions of these lattice defects, and of the interaction both between these defects and with many order parameters. Here, we report how such information can, for the first time, be obtained from a sample of $LuFe_2O_{4.22}$ using a range of techniques including advanced electron microscopy, atomic-resolution spectroscopy, and density functional theory calculations. The results provide quantitative atomic details of the crystal unit cell, together with a description of the ferroelastic, ferroelectric, and ferromagnetic order parameters. We elucidate also the interaction between these order parameters and the positions of the oxygen interstitials in the oxygen-enriched sample. The comprehensive analysis of oxygen interstitial ordering provides insights into understanding the coupling among different degrees of freedom in rare earth ferrites and demonstrates that oxygen content regulation is a powerful tool for tuning the microstructure and properties for this class of quantum material.

DOI: 10.1103/PhysRevLett.123.247601

Order parameters, which measure the degree of order in a phase transition system, and which usually diverge at the critical point, are closely related to various important materials properties. For example, a strong coupling between different order parameters accounts for many exotic phenomena, such as superconductivity and multiferroicity [1–6]. Moreover, the dependence of various order parameters on the atomic structure provides the possibility to modulate properties by the introduction of lattice defects [7–10]. Understanding how lattice defects can influence multiple order parameters is therefore of key importance for the design of materials with controlled functionality.

Among the possible lattice defects, oxygen interstitials or vacancies play a special role in modulating the microstructures and properties of oxides [11–16]. However, many of the underlying mechanisms remain elusive, including the importance of the precise position and ordering characteristics of interstitial atoms and/or vacancies, the interaction between these lattice defects and the lattice atoms in the primitive cell, and the influence of any coupling between the various order parameters that are dependent on the lattice defects. A good model system for the study of these questions is the rare earth ferrite $LuFe_2O_4$, as this material has a high tolerance for different oxygen stoichiometries, and its properties are sensitive to the specific oxygen content [17–21]. Because of the coexistence of Fe^{2+} and Fe^{3+}, the oxygen content can vary in this material as $LuFe_2O_{4+x}$ with $-0.5 \leq x \leq 0.5$ [18,21,22]. Different oxygen contents result in different structures, each of which can be classified by a modulation vector describing the local ordering [21]. For example, a second-order modulation observed recently in $LuFe_2O_{4+x}$ was also presumed to be caused by the presence of oxygen interstitials [23]. Direct experimental evidence of the correlation between the abundance of modulation structures and oxygen interstitial content is, however, still lacking.

By annealing $LuFe_2O_4$ in a controlled atmosphere, an oxygen-rich heavily hole-doped composition of $LuFe_2O_{4+x}$ can be synthesized (where later in this article,

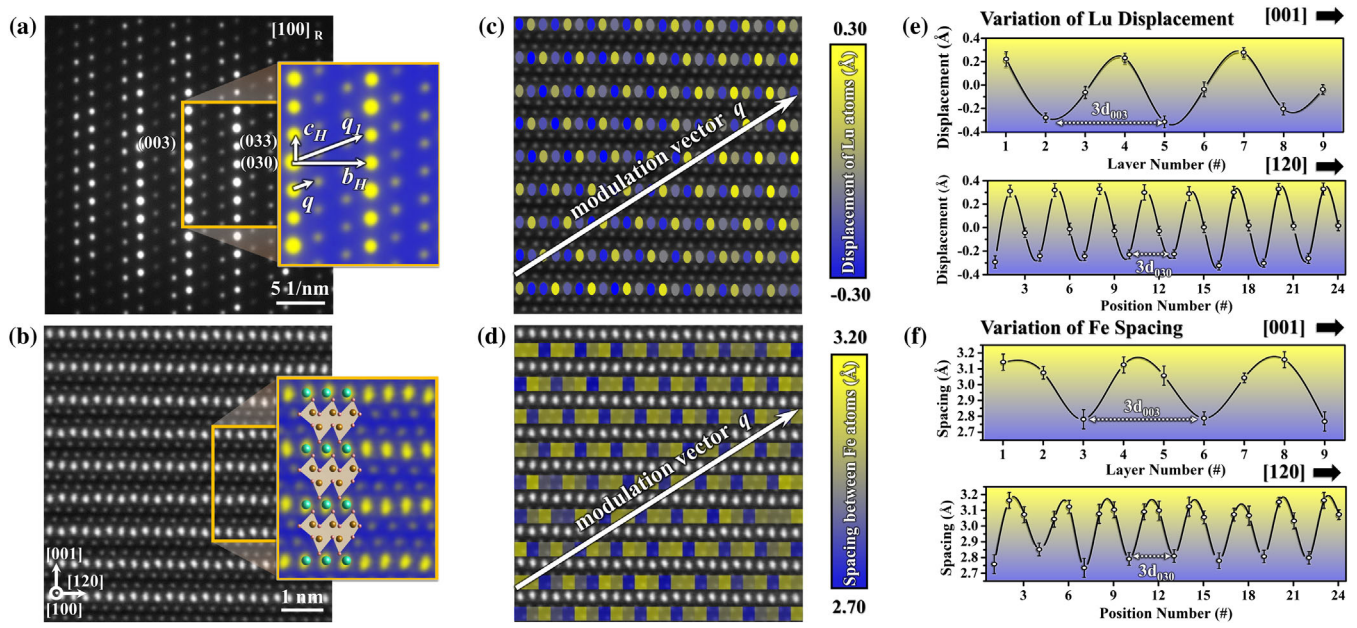

FIG. 1. Modulation structure in diffraction pattern and HAADF image. (a) Diffraction pattern along the [100] zone axis; the inset shows the relationship between the modulation vector $\boldsymbol{q}$ and vector $\boldsymbol{q}_1$. (b) HAADF image along the [100] zone axis. The enlargement highlights the [*AAA*] stacking sequence, consistent with the atomic model. Green, brown, and red atoms represent Lu, Fe, and O atoms, respectively. (c),(d) Maps showing the periodic variation of the Lu displacement and Fe spacing. (e),(f) Variation of the Lu displacement and the Fe spacing along the [001] and [120] directions, respectively.

we show that $x = 0.22$). By the study of this material we directly reveal for the first time oxygen interstitial ordering in the compound $LuFe_2O_{4.22}$. This is combined with a characterization of the introduced order parameters, including lattice, charge, and spin, through direct atomic imaging of oxygen interstitials, high angular annular dark field (HAADF) imaging, atomic-resolution electron-energy loss spectroscopy (EELS), and density functional theory (DFT) calculations. We show that ordering of the oxygen interstitials causes periodic displacements of the Lu and Fe atoms, associated with a new type of charge ordering and spin configuration, consistent with the modulation structure revealed from experimental electron diffraction pattern measurements.

Figure 1(a) is a selected area electron diffraction pattern taken along the [100] crystal axis. Superlattice diffraction spots are seen lying along the direction parallel to the white arrow in figure connecting the (000) and (033) diffraction spots. Denoting this arrow vector as $\boldsymbol{q}$ and taking $\boldsymbol{q_1} = (033)^*$ [see inset in Fig. 1(a)], we can write $\boldsymbol{q} \approx 0.33\boldsymbol{q}_1$. When defined with respect to the horizontal $\boldsymbol{b}_H = (030)^*$ and vertical $\boldsymbol{c}_H = (003)^*$ reciprocal lattice vectors, the vector $\boldsymbol{q}$ can be written as $0.33\boldsymbol{b}_H + 0.33\boldsymbol{c}_H$. It will be shown below that the vector $\boldsymbol{q}$ is a modulation vector that describes the modulated structure resulting from the interstitial oxygen. Further examples of diffraction patterns taken along different zone axes are shown in the Supplemental Material, Fig. S2 [24].

A HAADF image taken along the [100] zone axis of the $LuFe_2O_{4.22}$ sample is shown in Fig. 1(b). The contrast in the image derives primarily from atomic number variations, with an unobservable signal from oxygen atoms, and where atoms with a larger atomic number (Z) appear brighter. When the oxygen exceeds a certain level [17,18,21], the $FeO-LuO_2-FeO$ unit layer glides $\frac{1}{3}(030)$ in the [120] direction so that the stacking type transforms from [*ABC*] to [*AAA*] (see Fig. S1 [24] for more descriptions of these two stacking types). This is also confirmed in our sample, as shown in the enlarged image in Fig. 1(b), where the corresponding atomic model highlights the [*AAA*] stacking. These real space images contain information regarding periodic displacements of the Lu and Fe atoms. By accurate measurement of the atom positions, we obtained the displacements of the Lu atoms and the spacing between neighboring Fe atoms, and find that both of these show periodic variations along the direction of the vector $\boldsymbol{q}$, as shown in Figs. 1(c) and 1(d). The characteristic length of the periodic variations for both the Lu displacement and the Fe spacing, along the [001] and [120] directions, respectively, are in each case three times the atomic spacing along the corresponding crystal directions. This is consistent with the components of the vector $\boldsymbol{q}$ determined with respect to the $\boldsymbol{b}_H$ and $\boldsymbol{c}_H$ vectors in diffraction patterns [see Figs. 1(e) and 1(f)]. Accordingly, we can see that $\boldsymbol{q}$ is also a modulation vector for the lattice fluctuations of both the Lu and Fe atoms. Additional HAADF images acquired along different zone axes are shown in Fig. S3 [24].

As the HAADF image does not provide information about the doped oxygen atom positions, we use integrated

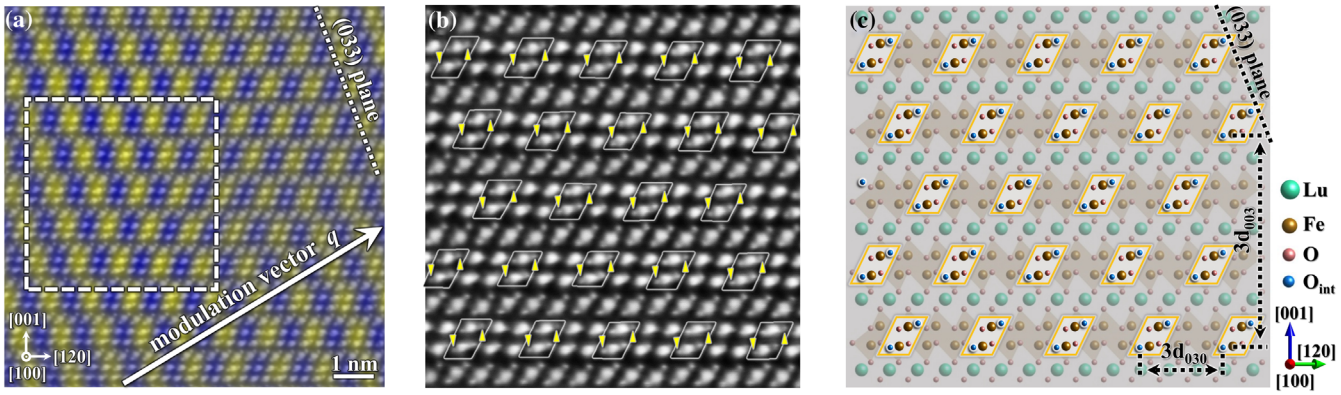

FIG. 2. IDPC image showing the oxygen interstitials. (a) IDPC image along a [100] zone axis; yellow coloring represents areas with oxygen interstitials. (b) Enlargement of the white dashed rectangle in (a) showing clearly the accurate positions of oxygen interstitials, indicated by yellow arrows. (c) Corresponding atomic model where the interstitial oxygens are represented by blue spheres.

differential phase contrast (IDPC) in the scanning transmission electron microscope (STEM), which has a high sensitivity to both heavy and light atoms. In an IDPC image the contrast correlates approximately linearly with the potential, which in turn is directly proportional to the projected electrostatic potential field of a thin sample, with clear maxima at the atomic positions [34–36]. Figure 2 shows an IDPC image along the [100] zone axis. In Fig. 2(b), the oxygen interstitials can be easily identified, where it is seen that they are located between the [FeO] and [LuO_2] layers on both sides of the FeO bilayer, as indicated by the yellow arrows. By identifying the positions of all the oxygen interstitials in Fig. 2(a) [present in the yellow areas of Fig. 2(a) and highlighted by arrows in Fig. 2(b)], it is found that they are located on the (033) plane and exhibit a periodic arrangement along the direction of the modulation vector $\boldsymbol{q}$. The characteristic lengths of this periodic arrangement are 3× the spacing along the [001] and [120] directions, as shown by $3d_{003}$ and $3d_{030}$ in the corresponding atomic model in Fig. 2(c). Therefore, the modulation vectors for the oxygen interstitial ordering, as well as for the metal atom displacements and for the periodicity of the superlattice diffraction spots are all identical, and are described by $\boldsymbol{q} \approx 0.33\boldsymbol{q}_1$.

The modulation in charge ordering has also been analyzed using atomic-column resolved EELS. Example images together with corresponding EELS spectra are shown in Figs. 3(a)–3(c). It is instructive to analyze separately the results corresponding to the two Fe atom layers, as indicated in Fig. 3(b), where six representative Fe atom positions in layers I and II are marked. The signals from the Fe L edge and the O K edge of these different positions are shown in Figs. 3(d)–3(g), labeled corresponding to the numbering in Fig. 3(b). Considering initially layer I [EELS spectra shown in Figs. 3(d) and 3(e)], the Fe $L_{3,2}$ edge shows a chemical shift, where the energy loss for Fe atoms at positions 3 and 6 are shifted to lower energies than for atoms at other positions. Comparing this result with the atomic displacements seen in the HAADF images, the chemical shift reveals that Fe atoms bonded to oxygen interstitials have a higher valence than those not bonded to the O interstitial. In the O K edge signal, the energy loss peak at 530 eV is weaker at positions 3 and 6 than at other positions. As the energy loss peak at near 530 eV represents hybridization between O and Fe [37], this implies enhanced Fe-O hybridization at positions 1, 2, 4, and 5, in agreement with the metal atom displacements observed in the HAADF images, and the observation that the oxygen interstitials are located between positions 1 and 2, and positions 4 and 5. We can conclude, therefore, that the Fe atoms at positions 1, 2, 4, and 5 tend to form FeO_6 coordination, while only FeO_5 coordination is present at positions 3 and 6. The higher oxygen coordination of Fe atoms at positions 1, 2, 4, and 5 explains the observed chemical shift of the Fe $L_{2,3}$ edge at these positions, related to the higher valence.

A similar analysis is carried out for layer II. In this layer [Figs. 3(f) and 3(g)], the Fe $L_{2,3}$ edge at positions 2 and 5 is shifted to lower energy and a weaker peak near 530 eV for the O K edge is found at these positions. Therefore, it can be concluded that the oxygen interstitials in layer II are located near positions 1 and 6, and between positions 3 and 4 (with no interstitial near positions 2 or 5), which is also consistent with the oxygen interstitial ordering presented in Fig. 2. The variation in Fe atoms valence can also be demonstrated by calculation of the $L_{3,2}$ ratios [38–40], as shown in Figs. 3(h) and 3(i), where the $L_{3,2}$ ratios for other layers in the spectrum image of Fig. 3(c) are calculated from the extracted Fe L edge signals (see also Fig. S7 [24]).

Combining both the variations in Fe atom and the ordering of oxygen interstitial atoms, it is revealed that a new charge ordering is formed, which matches the periodicity of the modulation vector $\boldsymbol{q}$, as shown in Fig. 3(i).

Based on our experimental results an initial supercell including the oxygen interstitial positions was constructed for DFT optimization, with size is equivalent to $3 \times 3 \times 3$ hexagonal unit cells of $LuFe_2O_4$, with the stacking

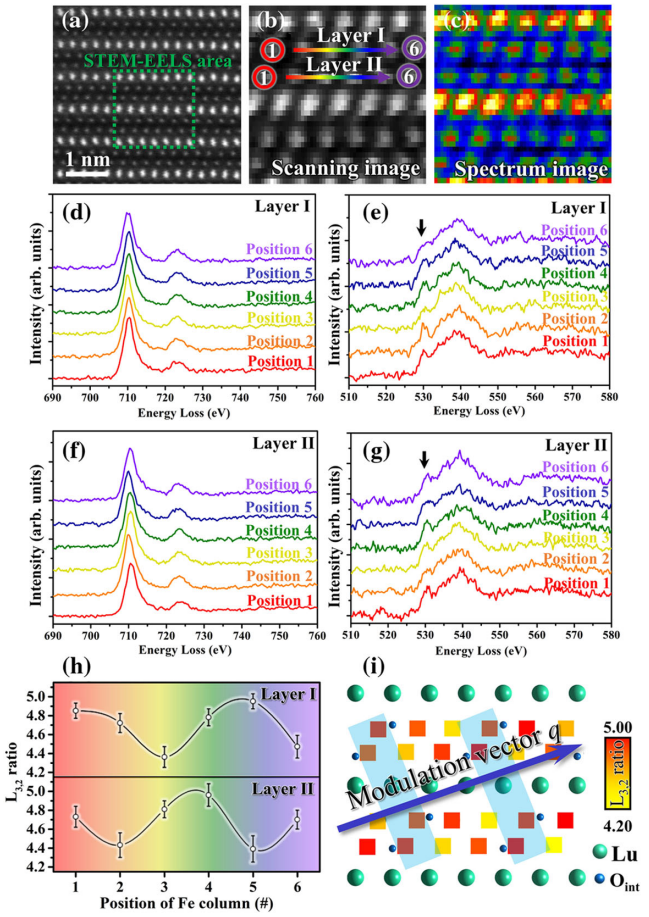

FIG. 3. Atomic-column resolved EELS results. (a) HAADF image along the [100] zone axis. The green dashed rectangle represents the STEM-EELS acquiring area. (b),(c) Scanning image and spectrum image of the EELS acquisition area. (d), (e) EELS signals for the Fe L edge and O K edge in layer I. Different colors represent the different acquisition positions shown in the scanning image (b). The black arrow in (e) indicates the peak of the O K edge around 530 eV. (f),(g) EELS signals for the Fe L edge and O K edge in layer II. (h) $L_{3,2}$ ratios for different positions in layers I and II calculated from the Fe L edge signals and (i) map of $L_{3,2}$ ratios for different atomic positions, showing the modulation vector $\boldsymbol{q}$.

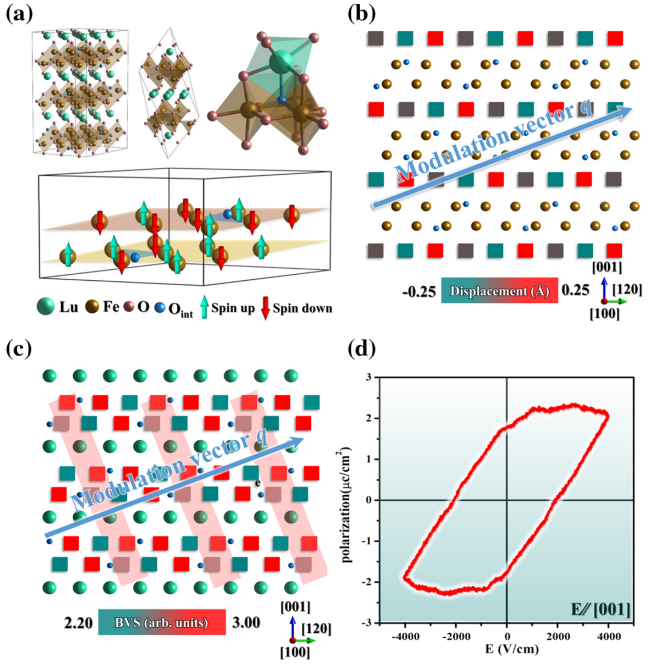

FIG. 4. Lattice, spin and charge structures of $LuFe_2O_{4.22}$. (a) Supercell of $LuFe_2O_{4.22}$ and a reduced supercell with rhombohedral symmetry. The coordination between metal atoms and oxygen interstitial is also shown in the magnified image. Blue spheres represent oxygen interstitials. The spin configuration of the lowest energy AF-II state is shown in the lower part of the figure. Arrows with different colors represent different spin directions in the neighboring layers, respectively. (b) Calculated displacement of Lu atoms along the [001] direction of the AF-II magnetic structure; the projection direction is the [100] zone axis. (c) Average bond valence sum of each Fe column for the structure with AF-II structure. (d) Room-temperature polarization-electric field loops for $LuFe_2O_{4.22}$, demonstrating robust and switchable ferroelectricity.

sequence changed from [*ABC*] to [*AAA*], see Fig. 4(a). This supercell can be regard as a rhombohedral structure where the primitive cell contains 9 Lu atoms, 18 Fe atoms, and 38 O atoms, giving a stoichiometry of $LuFe_2O_{4.22}$, also shown in Fig. 4(a). All DFT calculations were performed using this primitive cell, with the oxygen interstitials forming a simple cubic lattice with an average distance between oxygen interstitials of 7.4 Å. In the supercell model each interstitial oxygen is bonded to three Fe atoms, transforming what would be a FeO_5 bipyramid to an FeO_6 octahedron.

Although not exhaustive for this complex structure, various magnetic configurations were tested in the DFT calculations using this supercell, including ferromagnetism (F), ferrimagnetism (FM-I to FM-IV), and antiferromagnetism (AF-I to AF-IV); see Fig. S9 [24] for a further description of different spin configurations. After full relaxation, the lowest energy structure is AF-II [see the lower part of Fig. 4(a)]. There are nine Fe atoms within each magnetic atomic layer. For the AF-II configuration, there are three spin-up atoms and six spin-down atoms in one layer, but six spin-up and three spin-down atoms in the neighboring layer (Fig. S10 [24] shows the AF-II configurations viewed along [001] zone axis). The calculations give negligible net magnetic moment for the lowest energy state (AF-II) within numerical accuracy. This can be compared with the net magnetic moment of 2.33 μ_B per formula unit (f.u.) for fully stoichiometric $LuFe_2O_4$, which exhibits ferrimagnetism. After full relaxation, the Lu and Fe atoms adjacent to the oxygen interstitials are displaced towards the oxygen interstitials, as shown in Fig. 4(c). The calculated displacement of the Lu and Fe atoms [Fig. 4(b) and Fig. S11 [24]] agree well with the experimental measurements taken from the HAADF images, both regarding periodicity and

magnitude. The simulation results, including reciprocal and real space images are shown in Fig. S12 [24]. Good agreement is seen in each case with the corresponding experimental images.

To further elucidate the order coupling we also analyzed the valence states of the Fe ions according to their bond valence sum (BVS) [41], local magnetic moment, and Bader charge. As shown in Table S2 [24], the Fe ions can be divided into two types, corresponding to Fe^{2+} and Fe^{3+}. The Fe atoms close to oxygen interstitials have higher valence, whereas those located at other positions have a lower valence. Figure 4(c) shows the charge ordering for the Fe atoms, where it is seen that viewed along the [100] zone axis the average valence of the Fe column near the oxygen interstitials is higher than for other columns, which is consistent with the experimental EELS results. Compared with stoichiometric $LuFe_2O_4$, the presence of oxygen interstitials in $LuFe_2O_{4.22}$ increases the number of Fe^{+3} atoms, resulting in a Fe^{3+}/Fe^{2+} ratio of 13:5 in $LuFe_2O_{4.22}$ compared to just 1:1 in fully stoichiometric $LuFe_2O_4$.

Compared with its stoichiometric counterpart, the oxygen-rich $LuFe_2O_{4.22}$ is heavily hole doped. Surprisingly, the material remains insulating in the presence of this new form of charge ordering, as revealed by density of states (DOS) calculations (Fig. S13 [24]). We performed structural relaxation with both noncentrosymmetric space group $R3m$ and centrosymmetric space group $R\bar{3}m$. After full relaxation, the structure with the lowest energy is Cm, with AF-II spin configuration (see Table S3 [24] for comparisons of the total energies between different symmetries). Using Cm as a ferroelectric phase and $R\bar{3}m$ as a paraelectric phase, the spontaneous electric polarization was calculated by summation of the contributions from each atom, as the product of the displacement of each atom and its Born effective charge (BEC) (Fig. S14 [24]). The BEC's were calculated with density functional perturbation theory [42–44], as shown in Table S4 [24]. The calculated value for the electric polarization is 0.46 $\mu C/cm^2$.

It has been proposed previously that stoichiometric $LuFe_2O_4$ is a prototypical example of a charge-order (CO) based ferroelectric material [45], with the equal amounts of Fe^{2+} and Fe^{3+} in adjacent layers forming a triangular polar sublattice (W layer). However, direct experimental verification of ferroelectricity in $LuFe_2O_4$ has been elusive to date [46]. In our $LuFe_2O_{4.22}$ sample, the atomic displacements and the changes in the number of bivalent Fe^{2+} and trivalent Fe^{3+} iron ions alter the polar structure accordingly. Interestingly, $LuFe_2O_{4.22}$ displays a clear ferroelectric polarization loop [Fig. 4(d)]. Together with the theoretical calculations based on the accurately measured atomic positions the polarization measurement indicates the presence of switchable ferroelectric polarization in hole-doped $LuFe_2O_{4.22}$.

Summary.—In conclusion, the oxygen interstitial ordering in oxygen-doped $LuFe_2O_4$, with a structure and composition determined as $LuFe_2O_{4.22}$, has been directly revealed for the first time. The oxygen interstitial ordering and related lattice, charge, and spin ordering form the new modulation structure, all described by the same modulation vector. We show that $LuFe_2O_{4.22}$ has good ferroelectric properties at room temperature and exhibits antiferromagnetism below 170 K, both of which are strong in contrast to the behavior of undoped $LuFe_2O_4$. The combined experimental and modeling results demonstrate how the oxygen interstitial ordering alters the properties of $LuFe_2O_{4+x}$ through the effect on multiple ordering parameters. The results presented here also provide a direct insight into the coupling mechanisms between multiple order parameters in oxygen-doped material.

This work was financially supported by the Chinese National Natural Science Foundation (51788104, 51390471, 51527803, 51525102, 51371102, 51390475, 51761135131, 11834009, 11504053), the National 973 Project of China (2015CB654902), the National Key Research and Development Program (2016YFB0700402, 2016YFA0300702), and the Program of Shanghai Academic Research Leader (Grant No. 17XD1400400). This work made use of the resources of the National Center for Electron Microscopy in Beijing, Shanghai Supercomputer Center, and Tsinghua National Laboratory for Information Science and Technology. Work at the Oak Ridge National Laboratory (M. A., B. C. S. and D. M.—as-grown crystals) was supported by the U.S. Department of Energy, Office of Science, Basic Energy Sciences, Materials Sciences and Engineering Division. The authors thank Professor Andy Godfrey (School of Materials Science and Engineering, Tsinghua University) for suggestions following a critical reading of the manuscript. Dr. Dongchang Wu from Shanghai Nanoport, Thermofisher Scientific is gratefully acknowledged for helpful assistance in acquiring the IDPC images.

The authors declare no competing interests.

*Author to whom correspondence should be addressed. jzhu@mail.tsinghua.edu.cn

†Author to whom correspondence should be addressed. ryu@tsinghua.edu.cn

‡Y. Z., W. W. and W. X. contributed equally to this work.

[1] D. V. Efremov, J. van den Brink, and D. I. Khomskii, Nat. Mater. **3**, 853 (2004).

[2] J. Zhao, Q. Huang, C. de la Cruz, S. L. Li, J. W. Lynn, Y. Chen, M. A. Green, G. F. Chen, G. Li, Z. Li, J. L. Luo, N. L. Wang, and P. C. Dai, Nat. Mater. **7**, 953 (2008).

[3] G. D. Liu, X. F. Dai, S. Y. Yu, Z. Y. Zhu, J. L. Chen, G. H. Wu, H. Zhu, and J. Q. Xiao, Phys. Rev. B **74**, 054435 (2006).

[4] P. Zavalij, Wei Bao, X. F. Wang, J. J. Ying, X. H. Chen, D. M. Wang, J. B. He, X. Q. Wang, G. F. Chen, P.-Y. Hsieh, Q. Huang, and M. A. Green, Phys. Rev. B **83**, 132509 (2011).

[5] S. B. Cheng, M. L. Li, S. Q. Deng, S. Y. Bao, P. Z. Tang, W. H. Duan, J. Ma, C. W. Nan, and J. Zhu, Adv. Funct. Mater. **26**, 3589 (2016).

[6] S. Deng, S. Cheng, M. Liu, and J. Zhu, ACS Appl. Mater. Interfaces **8**, 25379 (2016).

[7] Z. Lei *et al.*, Nature (London) **563**, 546 (2018).

[8] K. Vanheusden, C. H. Seager, W. L. Warren, D. R. Tallant, and J. A. Voigt, Appl. Phys. Lett. **68**, 403 (1996).

[9] A. Janotti and C. G. Van de Walle, Appl. Phys. Lett. **87**, 122102 (2005).

[10] Y.-J. Kim, R. Z. Tao, R. F. Klie, and D. N. Seidman, ACS Nano **7**, 732 (2013).

[11] S. Q. Deng, S. B. Cheng, C. S. Xu, B. H. Ge, X. F. Sun, R. Yu, W. H. Duan, and J. Zhu, ACS Appl. Mater. Interfaces **9**, 27322 (2017).

[12] L. Z. Li, X. X. Cheng, T. Blum, H. X. Huyan, Y. Zhang, C. Heikes, X. X. Yan, C. Gadre, T. Aoki, M. J. Xu, L. Xie, Z. J. Hong, C. Adamo, D. G. Schlom, L. Q. Chen, and X. Q. Pan, Nano Lett. **19**, 6812 (2019).

[13] D. Lee, *et al.*, Science **362**, 1037 (2018).

[14] P. Sharma, Z. Huang, M. S. Li, C. J. Li, S. B. Hu, H. Lee, J. W. Lee, C. B. Eom, S. J. Pennycook, J. Seidel, Ariando, and A. Gruverman, Adv. Funct. Mater. **28**, 1707159 (2018).

[15] D. S. Song, X. F. Zhang, C. S. Lian, H. Liu, I. Alexandrou, I. Lazic, G. T. Eric, Bosch, D. Zhang, L. L. Wang, R. Yu, Z. Y. Cheng, C. L. Song, X. C. Ma, W. H. Duan, Q. K. Xue, and J. Zhu, Adv. Funct. Mater. **29**, 1903843 (2019).

[16] D. A. Muller, N. Nakagawa, A. Ohtomo, J. L. Grazul, and H. Y. Hwang, Nature **430**, 657 (2004).

[17] M. D. Hervieu, F. Poienar, M. Elkaïm, E. Rouquette, J. Abakumov, A. M. Van Tendeloo, G. Maignan, and A. Martin, Solid State Sci. **23**, 26 (2013).

[18] M. Hervieu, F. Damay, A. Maignan, and C. Martin, Solid State Sci. **48**, A1 (2015).

[19] H. X. Yang, H. F. Tian, Y. Zhang, Y. B. Qin, L. J. Zeng, C. Ma, H. L. Shi, and J. B. Lu, Solid State Commun. **150**, 1467 (2010).

[20] J. Bourgeois, M. Hervieu, M. Poienar, A. M. Abakumov, E. Elkaïm, M. T. Sougrati, F. Porcher, F. Damay, J. Rouquette, G. Van Tendeloo, A. Maignan, J. Haines, and C. Martin, Phys. Rev. B **85**, 064102 (2012).

[21] M. G. Hervieu, A. Bourgeois, J. Elkaim, E. Poienar, M. Damay, F. Rouquette, J. Maignan, and A. Martin, Nat. Mater. **13**, 74 (2014).

[22] H. X. Yang, H. F. Tian, Z. Wang, Y. B. Qin, C. Ma, J. Q. Li, Z. Y. Cheng, R. Yu, and J. Zhu, J. Phys. Condens. Matter **24**, 435901 (2012).

[23] S. Q. Deng, L. J. Wu, H. Cheng, J. C. Zheng, S. B. Cheng, J. Li, W. B. Wang, J. Shen, J. Tao, J. Zhu, and Y. M. Zhu, Phys. Rev. Lett. **122**, 126401 (2019).

[24] See Supplemental Material at http://link.aps.org/supplemental/10.1103/PhysRevLett.123.247601 for Experimental section, Supplementary text, Figs. S1–S15, Tables S1–S4, including Refs. [17,21,25–33].

[25] P. Hohenberg and W. Kohn Phys. Rev. **136**, B864 (1964).

[26] P. E. Blöchl, Phys. Rev. B **50**, 17953 (1994).

[27] S. L. Dudarev, G. A. Botton, S. Y. Savrasov, C. J. Humphreys, and A. P. Sutton, Phys. Rev. B **57**, 1505 (1998).

[28] G. Kresse and J. Furthmüller, Phys. Rev. B **54**, 11169 (1996).

[29] G. Kresse and D. Joubert, Phys. Rev. B **59**, 1758 (1999).

[30] H. J. Monkhorst and J. D. Pack, Phys. Rev. B **13**, 5188 (1976).

[31] J. P. Perdew, K. Burke, and M. Ernzerhof, Phys. Rev. Lett. **77**, 3865 (1996).

[32] Y. Zhang, H. X. Yang, C. Ma, H. F. Tian, and J. Q. Li, Phys. Rev. Lett. **98**, 247602 (2007).

[33] P. A. Beck, J. Less-Common Met. **28**, 193 (1972).

[34] N. Shibata, S. D. Findlay, Y. Kohno, H. Sawada, Y. Kondo, and Y. Ikuhara, Nat. Phys. **8**, 611 (2012).

[35] I. Lazic, E. G. T. Bosch, and S. Lazar, Ultramicroscopy **160**, 265 (2016).

[36] H. H. Rose, U.S. Patent No. 3, 124 (1975).

[37] J. A. Mundy, Q. Mao, C. M. Brooks, D. G. Schlom, and D. A. Muller, Appl. Phys. Lett. **101**, 042907 (2012).

[38] H. K. Schmid and W. Mader, Micron **37**, 426 (2006).

[39] P. A. L. van Aken and B. Liebscher, Phys. Chem. Miner. **29**, 188 (2002).

[40] H. Tan, J. Verbeeck, A. Abakumov, and G. V. Tendeloo, Ultramicroscopy **116**, 24 (2012).

[41] N. E. Brese and M. O'Keeffe, Acta Crystallogr. Sect. B **47**, 192 (1991).

[42] M. Gajdoš, K. Hummer, G. Kresse, J. Furthmüller, and F. Bechstedt, Phys. Rev. B **73**, 045112 (2006).

[43] N. A. Spaldin, J. Solid State Chem. **195**, 2 (2012).

[44] X. Gonze and C. Lee, Phys. Rev. B **55**, 10355 (1997).

[45] X. S. Xu, M. Angst, T. V. Brinzari, R. P. Hermann, J. L. Musfeldt, A. D. Christianson, D. Mandrus, B. C. Sales, S. McGill, J.-W. Kim, and Z. Islam, Phys. Rev. Lett. **101**, 227602 (2008).

[46] H. J. Xiang and M. H. Whangbo, Phys. Rev. Lett. **98**, 246403 (2007).